A SPectroscopic Survey of Biased Halos in the Reionization Era (ASPIRE): JWST Reveals a Filamentary Structure around a $z = 6.61$ Quasar

Feige Wang[1], Jinyi Yang[1,40], Joseph F. Hennawi[2,3], Xiaohui Fan[1], Fengwu Sun[1], Jaclyn B. Champagne[1],
Tiago Costa[4], Melanie Habouzit[5,6], Ryan Endsley[7], Zihao Li[8], Xiaojing Lin[8], Romain A. Meyer[9],
Jan–Torge Schindler[3], Yunjing Wu[1,8], Eduardo Bañados[9], Aaron J. Barth[10], Aklant K. Bhowmick[11], Rebekka Bieri[12],
Laura Blecha[11], Sarah Bosman[9], Zheng Cai[8], Luis Colina[13,14], Thomas Connor[15,16], Frederick B. Davies[9],
Roberto Decarli[17], Gisella De Rosa[18], Alyssa B. Drake[19], Eiichi Egami[1], Anna-Christina Eilers[20,41],
Analis E. Evans[11], Emanuele Paolo Farina[21], Zoltan Haiman[22,23], Linhua Jiang[24,25], Xiangyu Jin[1],
Hyunsung D. Jun[26], Koki Kakiichi[27], Yana Khusanova[9], Girish Kulkarni[28], Mingyu Li[8], Weizhe Liu[1],
Federica Loiacono[17], Alessandro Lupi[29], Chiara Mazzucchelli[30], Masafusa Onoue[25,31], Maria A. Pudoka[1],
Sofía Rojas-Ruiz[32,42], Yue Shen[33,34], Michael A. Strauss[35], Wei Leong Tee[1], Benny Trakhtenbrot[36],
Maxime Trebitsch[37], Bram Venemans[3], Marta Volonteri[38], Fabian Walter[9], Zhang-Liang Xie[9], Minghao Yue[1,20],
Haowen Zhang[1], Huanian Zhang[39], and Siwei Zou[8]

[1] Steward Observatory, University of Arizona, 933 North Cherry Avenue, Tucson, AZ 85721, USA; feigewang@email.arizona.edu
[2] Department of Physics, University of California, Santa Barbara, CA 93106-9530, USA
[3] Leiden Observatory, Leiden University, Niels Bohrweg 2, NL-2333 CA Leiden, The Netherlands
[4] Max-Planck-Institut für Astrophysik, Karl-Schwarzschild-Straße 1, D-85748 Garching b. München, Germany
[5] Zentrum für Astronomie der Universität Heidelberg, ITA, Albert-Ueberle-Str. 2, D-69120 Heidelberg, Germany
[6] Max-Planck-Institut für Astronomie, Königstuhl 17, D-69117 Heidelberg, Germany
[7] Department of Astronomy, The University of Texas at Austin, Austin, TX 78712, USA
[8] Department of Astronomy, Tsinghua University, Beijing 100084, People's Republic of China
[9] Max Planck Institut für Astronomie, Königstuhl 17, D-69117, Heidelberg, Germany
[10] Department of Physics and Astronomy, 4129 Frederick Reines Hall, University of California, Irvine, CA 92697-4575, USA
[11] Department of Physics, University of Florida, Gainesville, FL 32611, USA
[12] Center for Space and Habitability, University of Bern, Gesellschaftsstrasse 6 (G6), Bern, Switzerland
[13] Centro de Astrobiología (CAB), CSIC-INTA, Ctra. de Ajalvir km 4, Torrejón de Ardoz, E-28850, Madrid, Spain
[14] International Associate, Cosmic Dawn Center (DAWN), Denmark
[15] Center for Astrophysics | Harvard & Smithsonian, 60 Garden Street, Cambridge, MA 02138, USA
[16] Jet Propulsion Laboratory, California Institute of Technology, 4800 Oak Grove Drive, Pasadena, CA 91109, USA
[17] INAF–Osservatorio di Astrofisica e Scienza dello Spazio, via Gobetti 93/3, I-40129, Bologna, Italy
[18] Space Telescope Science Institute, 3700 San Martin Drive, Baltimore, MD 21210, USA
[19] Centre for Astrophysics Research, Department of Physics, Astronomy and Mathematics, University of Hertfordshire, Hatfield AL10 9AB, UK
[20] MIT Kavli Institute for Astrophysics and Space Research, 77 Massachusetts Avenue, Cambridge, MA 02139, USA
[21] Gemini Observatory, NSF's NOIRLab, 670 North A'ohoku Place, Hilo, HI 96720, USA
[22] Department of Astronomy, Columbia University, New York, NY 10027, USA
[23] Department of Physics, Columbia University, New York, NY 10027, USA
[24] Department of Astronomy, School of Physics, Peking University, Beijing 100871, People's Republic of China
[25] Kavli Institute for Astronomy and Astrophysics, Peking University, Beijing 100871, People's Republic of China
[26] SNU Astronomy Research Center, Seoul National University, 1 Gwanak-ro, Gwanak-gu, Seoul 08826, Republic of Korea
[27] Department of Physics, Broida Hall, University of California, Santa Barbara, CA 93106-9530, USA
[28] Tata Institute of Fundamental Research, Homi Bhabha Road, Mumbai 400005, India
[29] Dipartimento di Fisica "G. Occhialini", Università degli Studi di Milano-Bicocca, Piazza della Scienza 3, I-20126 Milano, Italy
[30] Instituto de Estudios Astrofísicos, Facultad de Ingeniería y Ciencias, Universidad Diego Portales, Avenida Ejercito Libertador 441, Santiago, Chile
[31] Kavli Institute for the Physics and Mathematics of the Universe (Kavli IPMU, WPI), The University of Tokyo, Chiba 277-8583, Japan
[32] Max-Planck-Institut für Astronomie, Königstuhl 17, D-69117, Heidelberg, Germany
[33] Department of Astronomy, University of Illinois at Urbana-Champaign, Urbana, IL 61801, USA
[34] National Center for Supercomputing Applications, University of Illinois at Urbana-Champaign, Urbana, IL 61801, USA
[35] Department of Astrophysical Sciences, Princeton University, Princeton, NJ 08544 USA
[36] School of Physics and Astronomy, Tel Aviv University, Tel Aviv 69978, Israel
[37] Kapteyn Astronomical Institute, University of Groningen, P.O. Box 800, 9700 AV Groningen, The Netherlands
[38] Institut d'Astrophysique de Paris, Sorbonne Université, CNRS, UMR 7095, 98 bis bd Arago, F-75014 Paris, France
[39] Department of Astronomy, Huazhong University of Science and Technology, Wuhan, 430074, People's Republic of China

---

[40] Strittmatter Fellow.
[41] Pappalardo Fellow.
[42] Fellow of the International Max Planck Research School for Astronomy and Cosmic Physics at the University of Heidelberg (IMPRS-HD).

Abstract

We present the first results from the JWST program A SPectroscopic survey of biased halos In the Reionization Era (ASPIRE). This program represents an imaging and spectroscopic survey of 25 reionization-era quasars and their environments by utilizing the unprecedented capabilities of NIRCam Wide Field Slitless Spectroscopy (WFSS) mode. ASPIRE will deliver the largest ($\sim$280 arcmin^2) galaxy redshift survey at 3–4 μm among JWST Cycle 1 programs and provide extensive legacy values for studying the formation of the earliest supermassive black holes, the assembly of galaxies, early metal enrichment, and cosmic reionization. In this first ASPIRE paper, we report the discovery of a filamentary structure traced by the luminous quasar J0305–3150 and 10 [O III] emitters at $z = 6.6$. This structure has a 3D galaxy overdensity of $\delta_{gal} = 12.6$ over 637 cMpc^3, one of the most overdense structures known in the early universe, and could eventually evolve into a massive galaxy cluster. Together with existing VLT/MUSE and ALMA observations of this field, our JWST observations reveal that J0305–3150 traces a complex environment where both UV-bright and dusty galaxies are present and indicate that the early evolution of galaxies around the quasar is not simultaneous. In addition, we discovered 31 [O III] emitters in this field at other redshifts, $5.3 < z < 6.7$, with half of them situated at $z \sim 5.4$ and 6.2. This indicates that star-forming galaxies, such as [O III] emitters, are generally clustered at high redshifts. These discoveries demonstrate the unparalleled redshift survey capabilities of NIRCam WFSS and the potential of the full ASPIRE survey data set.

Unified Astronomy Thesaurus concepts: Early universe (435); Galaxies (573); Protoclusters (1297); Redshift surveys (1378); Supermassive black holes (1663)

1. Introduction

Quasars, powered by accreting supermassive black holes (SMBHs) with masses of 10^8–$10^{10} M_\odot$, have been observed up to $z = 7.6$ (Bañados et al. 2018; Yang et al. 2020a; Wang et al. 2021), deep into the epoch of reionization (EoR). How these quasars formed within the first billion years after the Big Bang is one of the most important open questions in astrophysics. Cosmological simulations suggest that billion-solar-mass SMBHs in the EoR formed in massive dark matter halos (e.g., Di Matteo et al. 2005; Springel et al. 2005) and grew through cold flow accretion (e.g., Di Matteo et al. 2012) and/or merging with other gas-rich halos (e.g., Li et al. 2007). As a consequence, these quasars are expected to be found in large-scale galaxy overdensities in the early universe (e.g., Costa et al. 2014), although a large variance in the number of galaxies around SMBHs is possible, as suggested by large-scale cosmological simulations (e.g., Habouzit et al. 2019).

Observationally, however, testing these theories has proven to be difficult, even with the largest ground-based telescopes and the Hubble Space Telescope (HST). Particularly, whether the most distant quasars are embedded in galaxy overdensities has been the topic of great debate. In the past two decades, extensive efforts (see Overzier 2016, for a review) have been made to search for star-forming galaxies around $z > 6$ quasars (e.g., Willott et al. 2005; Zheng et al. 2006; Kim et al. 2009; Morselli et al. 2014; Simpson et al. 2014). These works mostly use photometrically selected Lyman break galaxy (LBG) candidates as tracers. However, the large redshift uncertainty (i.e., $\Delta z \sim 1$ when only a few broadband filters are used) of photometrically selected LBGs could significantly dilute the overdensity signal. While spectroscopic follow-up observations of these LBGs can confirm or rule out galaxy overdensities, no consensus has been reached yet, as such studies are very challenging. To date, only a few $z \sim 6$ quasars have been confirmed to be living in megaparsec-scale (comoving) galaxy overdensities from extensive spectroscopic observations (Bosman et al. 2020; Mignoli et al. 2020; Meyer et al. 2022; Overzier 2022) with an extent similar to that of protoclusters, the progenitors of galaxy clusters (e.g., Overzier 2016). On the other hand,

the Atacama Large Millimeter/submillimeter Array (ALMA) has played a major role in characterizing the small-scale environment of the earliest quasars, which indicates that a fraction of quasars have close companion galaxies detected in [C II] emissions (e.g., Decarli et al. 2017; Venemans et al. 2019); however, whether the overdensity of ALMA-selected galaxies around quasars extends to megaparsec scales is still unclear (Meyer et al. 2022).

With the launch of the James Webb Space Telescope (JWST), we have finally entered the era where deep spectroscopic observations of large statistical samples of high-redshift galaxies are available. Recent JWST NIRCam (Rieke et al. 2005) Wide Field Slitless Spectroscopy (WFSS) observations of the ultraluminous quasar J0100+2802 at $z = 6.3$ (Wu et al. 2015) revealed that it resides in a galaxy overdensity traced by [O III] emitters (Kashino et al. 2022), demonstrating the transformative capability of JWST in studying the large-scale environment of high-redshift quasars. To resolve the long-standing open question of whether the earliest SMBHs reside in the most massive dark matter halos and inhabit large-scale galaxy overdensities, we designed the program A SPectroscopic survey of biased halos In the Reionization Era (ASPIRE; program ID 2078; PI: F. Wang) to search for Hβ+[O III] emitters in the fields of 25 quasars at $z > 6.5$ by utilizing the spectroscopic capabilities of NIRCam/WFSS (Greene et al. 2017).

In this paper, we provide a brief overview of the ASPIRE project and present the discovery of a filamentary structure traced by the quasar J030516.92–315055.9 (hereafter J0305–3150) and 10 [O III] emitters at $z \sim 6.6$. We also report the discovery of 31 additional [O III] emitters in this field with half of them clustered at $z \sim 5.4$ and 6.2. In Section 2, we present a brief program design of ASPIRE, JWST observations, and data reduction. In Section 3, we report on the line emitter search and the discovery of 41 [O III] emitters in this field, and in Section 4, we discuss the properties of the filamentary structure and complex environment of J0305–3150. Finally, we summarize our results in Section 5. Throughout the paper, we adopt a flat ΛCDM cosmology with $H_0 = 70$ km s^{-1} Mpc^{-1}, $\Omega_M = 0.3$, and $\Omega_\Lambda = 0.7$.

2. Program Overview, Observations, and Data Reduction

2.1. ASPIRE Program Overview and Observations

The science drivers of the ASPIRE program are to resolve the long-standing question of whether the earliest SMBHs reside in massive dark matter halos and inhabit galaxy overdensities, detect the stellar light from quasar host galaxies, understand the SMBH growth and AGN feedback, and constrain cosmic reionization and metal enrichment in the early universe. The NIRCam/WFSS, with unprecedented spectroscopic capabilities and remarkable imaging sensitivity and resolution, is ideal for these purposes. To put the $H\beta$ +[O III] lines of both quasars and physically associated galaxies at the sweet spot of NIRCam/WFSS sensitivity, we focus on quasars at $6.5 < z < 6.8$. The ASPIRE program targets 25 known quasars at $6.5 < z < 6.8$ having both high-resolution (i.e., $\lesssim 0\rlap{.}''5$) ALMA observations (e.g., Venemans et al. 2019) and high-quality optical-to-infrared spectra (e.g., Yang et al. 2020b, 2021). These quasars are selected from various ongoing quasar surveys (e.g., Wang et al. 2019a; Yang et al. 2019, 2020b; Bañados et al. 2021) and have a bolometric luminosity range of $0.5–5 \times 10^{47}$ erg s^{-1}.

Since the continua of high-z galaxies are not central for our science goals, and using both grisms or observing at multiple position angles would add significant observing overheads, ASPIRE only uses grism R for the WFSS observations. ASPIRE uses the F356W filter for the WFSS observation in the long-wavelength (LW) channel and the F200W filter simultaneously in the short-wavelength channel (SW). This setup enables us to perform a slitless galaxy redshift survey at $\sim3–4\,\mu$m and obtain extremely deep imaging at $2\,\mu$m. The resolving power of the NIRCam/WFSS observations is about $R \sim 1300–1600$ from 3 to 4 μm. The dispersion of the NIRCam/WFSS data for our configuration is about $10\,\text{Å}$ pixel^{-1}. The main observations are performed with a three-point INTRAMODULEX primary dither pattern, and each primary position includes two subpixel dithers. This gives a survey area of ~11 arcmin^2 for the imaging and slitless spectroscopy. We use the SHALLOW4 readout pattern with nine groups and one integration, which gives a total on-source exposure time of 2834.5 s. To maximize the sky area coverage, both NIRCam modules are used by ASPIRE. The quasar is put at a carefully designed position ($X_{\text{offset}} = -60\rlap{.}''5$, $Y_{\text{offset}} = 7\rlap{.}''5$) in module A to ensure that we have full WFSS wavelength coverage and a full imaging depth for the quasar.

To identify the sources that are responsible for the slitless spectra imprinted on the NIRCam detectors, one needs to get direct imaging along with the WFSS observations. In addition, some sources that fall outside of the NIRCam imaging field of view could also produce spectra on the detectors. Therefore, the so-called out-of-field images dithering along the WFSS dispersion direction are also needed. The direct and out-of-field imaging were performed with the same readout pattern as the main observations, with the F115W filter in the SW and the F356W filter in the LW. The combination of direct and out-of-field imaging gives a total exposure time of 1417.3 s in the quasar vicinity but 472.4 s at the edge of the field for the F115W and F356W bands. We also obtained NIRISS parallel imaging, which is not used here and will be presented in future work.

In this work, we focus on one of the ASPIRE fields, centered on the quasar J0305–3150, which was observed on 2022 August 12 with JWST. It is a luminous ($L_{\text{bol}} = 10^{47}$ erg s^{-1}) quasar and hosts an SMBH with a mass of $\sim10^9\,M_\odot$ at $z = 6.614$ (Venemans et al. 2013). High-resolution ($\sim0\rlap{.}''08 \times 0\rlap{.}''07$) ALMA observations of J0305–3150 indicate that it is hosted by a massive galaxy ($M_{\text{dyn}} \sim 3 \times 10^{10}\,M_\odot$) with a [C II]-based redshift of $z = 6.6139$ (Venemans et al. 2019). The ALMA observations and previous MUSE observations (Farina et al. 2017) identified three [C II] emitters and one Lyα emitter (LAE) in the quasar vicinity, indicating that J0305–3150 could inhabit a galaxy overdensity. Nevertheless, Ota et al. (2018) found that the narrowband imaging–selected LAEs in the J0305–3150 field mostly show an underdensity in the quasar vicinity, with a observing depth slightly shallower than that of the MUSE observation presented in Farina et al. (2017). In addition, HST program GO 15064 (PI: Caitlin Casey) observed J0305–3150 with ACS imaging in the F606W and F814W bands and WFC3 imaging in the F105W, F125W, and F160W bands, making J0305–3150 the only ASPIRE quasar field covered by existing multiband optical and infrared imaging from HST and an ideal target for early ASPIRE data analysis. The detailed description of the HST observations, data reduction, and characterization of selected LBGs is presented in Champagne et al. (2023).

2.2. NIRCam Imaging Data Reduction

We performed a careful reduction of the NIRCam images using version 1.8.3 of the JWST Calibration Pipeline[43](CAL-WEBB) with some additional steps as detailed below. We use the reference files (jwst_1015.pmap) from version 11.16.15 of the standard Calibration Reference Data System[44] (CRDS) to calibrate our data. Below, we briefly summarize our reduction procedures.

After CALWEBB stage 1, we masked objects and generated smooth background images for individual exposures. We measured the $1/f$ noise model on a row-by-row and column-by-column basis for each amplifier following the algorithm proposed by Schlawin et al. (2020). Then we ran the stage 2 pipeline on the $1/f$ noise model subtracted stage 1 outputs. To remove the extra detector-level noise features seen in the individual stage 2 outputs, we constructed a master median background for each combination of detector and filter based on all available exposures from the ASPIRE program. The master backgrounds were then scaled and subtracted for individual exposures. After that, we aligned the LW images to a reference catalog from the DESI Legacy Imaging Surveys[45] (Dey et al. 2019) and then aligned all SW images to the calibrated LW images using tweakwcs.[46] The purpose of this step is to remove astrometric offsets between different detectors, modules, and filters. The aligned and calibrated individual files were then passed through the CALWEBB stage 3 pipeline to create drizzled images. During the resampling step, we used a fixed pixel scale of $0\rlap{.}''0311$ for SW images and $0\rlap{.}''0315$ for LW images and adopted pixfrac = 1. The mosaicked images are further aligned to the reference catalog from the DESI Legacy Imaging Surveys for absolute astrometric calibration. Our procedure yields precise relative alignment (rms $\simeq 15$ mas) and absolute astrometric calibration

---

[43] https://github.com/spacetelescope/jwst
[44] https://jwst-crds.stsci.edu
[45] https://www.legacysurvey.org
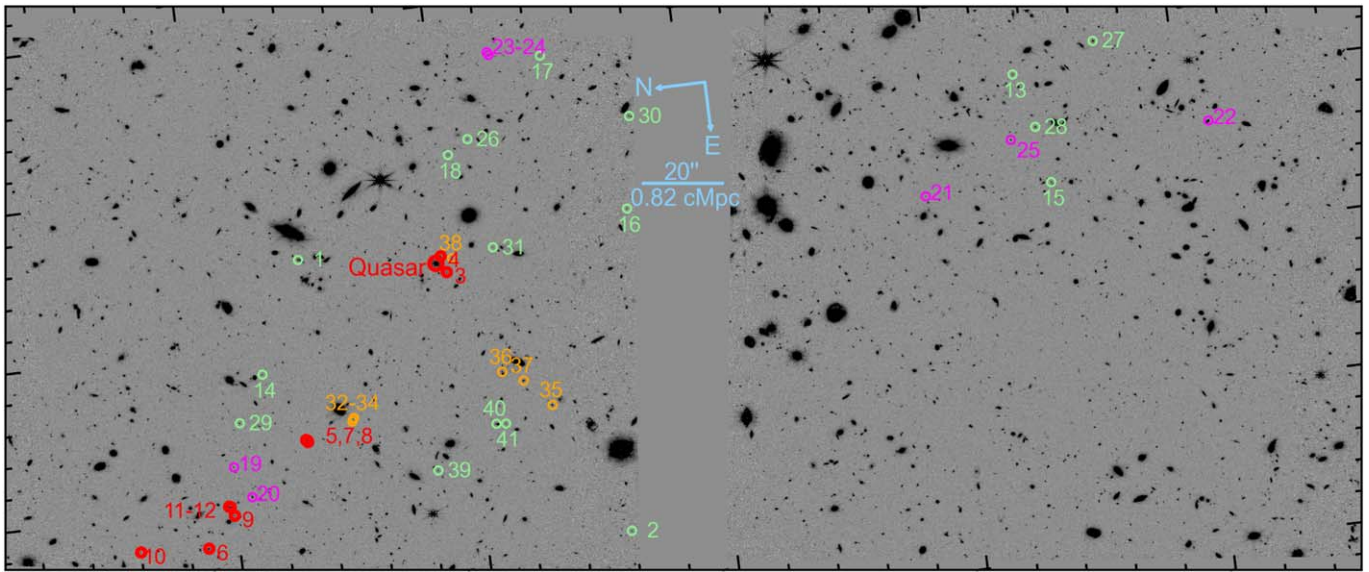[46] https://github.com/spacetelescope/tweakwcs

Figure 1. The F356W-band imaging of the J0305–3150 quasar field. We identified 41 [O III] emitters, as highlighted by colored circles. The quasar J0305–3150 and [O III] emitters with a line-of-sight velocity relative to the quasar of $\Delta v_{\rm los} < 1000$ km s^{-1} are highlighted by red circles. The magenta and orange circles denote the member galaxies of two galaxy overdensities at $z = 6.2$ and 5.4, respectively. The green circles are other field [O III] emitters. The compass and scale length (at $z = 6.6$) are shown as blue lines.

(rms $\simeq$ 50 mas). Finally, we derived and subtracted a background for each mosaic by utilizing the object detection and background estimation routines from `photutils`[47] to mask out objects and iteratively estimate the background. We then extracted a source catalog used for spectral extraction from the fully calibrated images using `SExtractor` (Bertin & Arnouts [1996]) with `DETECT_MINAREA = 5` and `DETECT_THRESH = 3`. The 5σ limiting magnitudes in the 0″32 diameter apertures of the calibrated images are 26.77, 27.48, and 27.85 AB magnitude for F115W, F200W, and F356W, respectively. To illustrate the quality of the NIRCam images, we show the F356W-band mosaic in Figure [1].

2.3. NIRCam WFSS Data Reduction

We used the `CALWEBB` stage 1 pipeline to calibrate the detector-level signals and ramp fitting for individual NIRCam WFSS exposures. After this step, we subtracted the $1/f$ noise pattern using the same routines that are used for the NIRCAM direct image processing, but we only subtracted the stripes along columns, since the spectra are dispersed along rows for grism R. We then performed flat-fielding of the WFSS exposures using direct imaging flat reference files, since the WFSS flat reference files are not available. We also assigned `WCS` information for individual files based on the distortion reference files in CRDS using the `assign_wcs` routine in the `CALWEBB` pipeline. We measured astrometric offsets between each of the SW images (i.e., the exposures taken simultaneously with WFSS exposures) and the fully calibrated F356W-band mosaic. The measured offsets were applied to the spectral tracing model in a later stage when tracing objects. All further data processing steps after this stage were performed using our custom scripts as detailed below.

In the standard `CALWEBB` pipeline, the WFSS background subtraction is performed by scaling the theoretical background to that observed in each individual integration. However, the accuracy of the theoretical background has not been fully characterized because of limited existing in-flight calibrations. To resolve this issue, we constructed median background models based on all ASPIRE observations obtained at similar times, which were scaled and subtracted from individual WFSS exposures.

Before extracting spectra from WFSS observations, we need to construct the spectral tracing models, dispersion models, and sensitivity functions. The methodology used for constructing these models is described in detail in Sun et al. ([2022a]). In this work, we used a spectral tracing model constructed using the spectral traces of point sources observed in the LMC field (PID 1076,) which has better detector coverage than that used in Sun et al. ([2022a], [2022b]), as well as updated sensitivity functions derived from Cycle 1 calibration programs (PIDs 1536, 1537, and 1538). The sensitivity functions measured from Early Release Observations and Cycle 1 calibration are consistent with each other to an accuracy of better than 2% over most wavelength coverage. We note that the dispersion and tracing models are measured from a different filter configuration and could have a small shift after considering different filter offsets. In the spatial direction (along columns for grism R), we measured a half-pixel offset between the model and our data. We cannot measure the offset along the dispersion direction (along rows for grism R), which requires in-flight observation of a wavelength calibrator and is not available yet. However, we expect that the constant offset will be small (<100 km s^{-1} or $\Delta z < 0.003$ for [O III] emitters), since the offset in the spatial direction is smaller than 1 pixel. Additionally, the redshift of one of the [O III] emitters is consistent with the galaxy's Lyα redshift ($z_{\rm [O\,III]} - z_{\rm Ly\alpha} = 0.002$; see Section [4.2]), and the redshift of the quasar derived from [O III] is also consistent with the quasar's [C II] redshift ($z_{\rm [O\,III]} - z_{\rm [C\,II]} = 0.001$; Yang et al. [2023]). Such a small wavelength zero-point offset does not affect any scientific results presented here.

With the models described above, we then extracted both 2D and 1D spectra for all sources ($\sim$5000) detected in the F356W direct imaging (Section [2.2]). We extracted two versions of

---

[47] https://photutils.readthedocs.io

spectra for each object. For the first version, we extracted the 1D spectra from individual WFSS exposures using both boxcar and optimal extraction algorithms (Horne 1986). The extracted individual 1D spectra were then combined with inverse variance weighting and outlier rejection. For the second version, we first extracted 2D spectra for each source from each individual exposure and then stacked the 2D spectra after registering them to a common wavelength and spatial grid following the histogram2D technique implemented in the PypeIt software (Prochaska et al. 2020) to avoid interpolations. We then extracted 1D spectra from the stacked 2D spectra using both boxcar and optimal extraction algorithms. We used an aperture diameter of 5 pixels ($0''315$) for the boxcar spectral extraction. The pixel scales for both 1D and 2D spectra are resampled to be 10 Å pixel^{-1}. During the 1D spectral extraction process for both methods, we performed iterative background subtraction to subtract off the background residuals. We note that the two spectra sets agree well with each other, and we only used the second approach in this work by considering that the profile fitting used for optimal extraction is slightly better characterized in the stacked 2D spectra for very faint galaxies. In the highest-sensitivity regions of the slitless spectra, the 5σ emission line detection limit for a point source is estimated to be 2.0×10^{-18} erg s^{-1} cm^{-2} by integrating the spectra over 50 Å (i.e., $\sim 2\times$ spectral resolution). This corresponds to a 5σ line luminosity limit of 9.9×10^{41} erg s^{-1} at $z = 6.6$.

3. Discovery of 41 [O III] Emitters at $5.3 < z < 6.7$

Directly detecting the rest-frame optical [O III] $\lambda\lambda 4960$, 5008 emission lines from EoR galaxies had been impossible until the launch of JWST. Within the first JWST observations, there are five [O III] emitters identified at $z > 5$ from NIRSpec observations of the SMACS 0723 field (e.g., Carnall et al. 2023; Curti et al. 2023) and another four galaxies discovered from NIRCam WFSS observations of the P330-E standard star field (Sun et al. 2022a, 2022b). The more recent deep NIRCam WFSS observation of the J0100+2802 quasar field identified more than 100 [O III] emitters at $z > 5$, demonstrating the power of the NIRCam WFSS mode (Kashino et al. 2022). These [O III] emitters are powered by young stellar populations and have high Hβ+[O III] equivalent widths (EWs), moderately low metallicities, and high ionization states (e.g., Sun et al. 2022a; Matthee et al. 2022).

To search for [O III] emitters in the J0305–3150 field, we developed a set of scripts to automatically search for line emitters from the extracted 1D spectra. We first produced a median-filtered continuum model with a window size of 51 pixels (510 Å), which is subtracted from the optimally extracted spectrum. We then applied a peak-finding algorithm to search for all peaks with a signal-to-noise ratio (S/N) >3 and rejected peaks with the two nearest pixels having S/N < 1.5, which are mostly residuals from hot pixels or cosmic rays. For the remaining detected peaks, we performed a Gaussian fitting to measure the FWHM and S/N, where the S/N was measured directly from the continuum-subtracted spectrum by integrating pixels within $\pm 1 \times$ FWHM. In this step, we rejected lines with S/N < 5 and an FWHM wider than seven times the spectral resolution ($R \sim 25$ Å, or about 2.5 pixels) or narrower than half of the spectral resolution to further reject fake lines. For each detected emission line, we first assumed that it is the [O III] $\lambda 5008$ line and then measured the S/N of the [O III] $\lambda 4960$ line at the expected wavelength by

assuming that it has the same FWHM as [O III] $\lambda 5008$. We identified an object as an [O III] emitter candidate only if there is a $>2\sigma$ significance line detection at the expected wavelength. Finally, we visually inspected the spectra for all [O III] emitter candidates and identified 41 [O III] emitters in the J0305–3150 field in addition to the quasar. To check the robustness of our line emitter searching algorithm, we further visually inspected all extracted spectra (~ 5000 sources in total). From the visual inspection, we found that our automatic line emitter searching method recovers all of the [O III] emitters identified by eye.

The basic information of these [O III] emitters is listed in Table 1. These [O III] emitters span a redshift range of $5.3 < z < 6.7$, an [O III] luminosity range of $L_{\text{[O III]}4960,5008} = (1.2–12.4) \times 10^{42}$ erg s^{-1}, and a rest-frame EW range of $80\,\text{Å} \lesssim \text{EW}_{\text{[O III]}4960,5008} \lesssim 4100\,\text{Å}$. The $L_{\text{[O III]}4960,5008}$ was determined from Gaussian fitting of both the [O III] $\lambda 5008$ and [O III] $\lambda 4960$ lines, and the EW$_{\text{[O III]}}$ 4960, 5008 was estimated based on the Hβ+[O III] line fitting result and F356W-band photometry by assuming that f_λ in the continuum is a constant across the F356W passband. The positions of these galaxies are highlighted in Figure 1, and the JWST and HST imaging thumbnails and the extracted spectra of these galaxies are presented in Figure 2. In Figure 3, we show the redshift distribution of all [O III] emitters identified in the field. Obviously, most of these [O III] emitters are clustered at $z \sim 5.4$ (orange), 6.2 (magenta), and 6.6 (red). This indicates that we are seeing three galaxy overdensities in just one ASPIRE field. In particular, the galaxy overdensity at $z \sim 6.6$ coincides with the redshift of the quasar and has the most abundant galaxies, indicating that quasar J0305–3150 traces a significant galaxy overdensity. In the following sections, we will focus on the galaxy overdensity at $z \sim 6.6$; more detailed spectral energy distribution modeling and characterization of these [O III] emitters will be presented in a subsequent paper (J. Champagne et al. 2023, in preparation).

4. Discussion

4.1. An Overdense Filamentary Structure around Quasar J0305–3150

Our new JWST observations allow us to characterize the megaparsec-scale (comoving) environment of the $z = 6.6$ quasar J0305–3150 for the first time. Among the 41 [O III] emitters identified in the J0305–3150 field, there are 12 (emitters 1–12) at $z \sim 6.61$–6.67. In particular, 10 of them (emitters 3–12) have line-of-sight velocity separations from the quasar with $\Delta v_{\text{los}} < 1000$ km s^{-1} (or <9.4 cMpc; see the inset of Figure 3), with a projected distance of $10-550$ proper kpc or $80-4100$ comoving kpc relative to the quasar. The velocity dispersion along the line of sight of these 10 [O III] emitters is $\sigma_v = 250$ km s^{-1}, similar to that found in the overdensity traced by the quasar J0100+2802 at a lower redshift (Kashino et al. 2022). Additionally, these 10 [O III] emitters are distributed along a filamentary structure toward the luminous quasar. In the left panel of Figure 4, we show the zoom-in 3D structure of this galaxy overdensity. The filamentary structure extends at least 4.1 cMpc along the projected plane and 8.0 cMpc along the line-of-sight direction. This is consistent with the size of the protoclusters seen in cosmological simulations (e.g., Overzier et al. 2009).

To characterize the galaxy overdensity of this structure, we first measure its galaxy number density using a cylinder

Table 1
List of Identified [O III] Emitters

Name[a]	R.A.	Decl.	z[b]	$L_{\text{[O III]}4960,5008}$ 10^{42} erg s^{-1}	EW$_{\text{[O III]}4960,5008}$ Å
ASPIRE-J0305M31-O3-001	03:05:16.530	−31:50:22.663	6.669	12.39 ± 0.63	679 ± 35
ASPIRE-J0305M31-O3-002	03:05:22.444	−31:51:35.268	6.656	2.05 ± 0.41	500 ± 100
ASPIRE-J0305M31-O3-003	03:05:17.109	−31:50:58.253	6.636	3.87 ± 0.39	550 ± 56
ASPIRE-J0305M31-O3-004	03:05:16.793	−31:50:57.264	6.631	6.52 ± 0.47	468 ± 34
ASPIRE-J0305M31-O3-005	03:05:19.954	−31:50:19.274	6.624	4.27 ± 0.59	201 ± 28
ASPIRE-J0305M31-O3-006	03:05:21.785	−31:49:52.576	6.623	10.72 ± 0.89	600 ± 50
ASPIRE-J0305M31-O3-007	03:05:19.971	−31:50:19.589	6.623	2.94 ± 0.56	91 ± 17
ASPIRE-J0305M31-O3-008	03:05:19.996	−31:50:19.682	6.621	1.94 ± 0.44	78 ± 18
ASPIRE-J0305M31-O3-009	03:05:21.221	−31:49:59.745	6.619	3.56 ± 0.56	528 ± 83
ASPIRE-J0305M31-O3-010	03:05:21.697	−31:49:36.022	6.617	2.91 ± 0.29	1523 ± 153
ASPIRE-J0305M31-O3-011	03:05:21.048	−31:49:58.981	6.616	4.50 ± 0.73	189 ± 31
ASPIRE-J0305M31-O3-012	03:05:21.040	−31:49:58.662	6.615	1.45 ± 0.48	110 ± 36
ASPIRE-J0305M31-O3-013	03:05:14.691	−31:53:20.922	6.550	2.58 ± 0.68	404 ± 107
ASPIRE-J0305M31-O3-014	03:05:18.612	−31:50:10.651	6.542	2.59 ± 0.63	718 ± 175
ASPIRE-J0305M31-O3-015	03:05:16.825	−31:53:27.012	6.506	6.07 ± 1.20	1331 ± 264
ASPIRE-J0305M31-O3-016	03:05:16.326	−31:51:43.739	6.497	3.09 ± 0.63	678 ± 140
ASPIRE-J0305M31-O3-017	03:05:13.220	−31:51:27.269	6.496	2.08 ± 0.47	580 ± 133
ASPIRE-J0305M31-O3-018	03:05:14.891	−31:51:02.045	6.419	2.05 ± 0.25	751 ± 92
ASPIRE-J0305M31-O3-019	03:05:20.302	−31:50:01.008	6.298	2.30 ± 0.45	718 ± 141
ASPIRE-J0305M31-O3-020	03:05:20.911	−31:50:04.545	6.298	7.22 ± 0.58	392 ± 32
ASPIRE-J0305M31-O3-021	03:05:16.800	−31:52:56.271	6.292	1.77 ± 0.51	860 ± 250
ASPIRE-J0305M31-O3-022	03:05:16.025	−31:54:06.873	6.280	8.41 ± 1.30	253 ± 39
ASPIRE-J0305M31-O3-023	03:05:13.031	−31:51:14.492	6.262	1.23 ± 0.38	456 ± 141
ASPIRE-J0305M31-O3-024	03:05:13.088	−31:51:14.824	6.257	6.05 ± 0.61	835 ± 84
ASPIRE-J0305M31-O3-025	03:05:15.928	−31:53:18.545	6.253	6.59 ± 1.00	741 ± 113
ASPIRE-J0305M31-O3-026	03:05:14.633	−31:51:07.238	6.089	1.92 ± 0.34	864 ± 154
ASPIRE-J0305M31-O3-027	03:05:14.240	−31:53:41.306	6.081	3.10 ± 1.08	161 ± 56
ASPIRE-J0305M31-O3-028	03:05:15.738	−31:53:24.841	6.078	2.79 ± 0.59	269 ± 57
ASPIRE-J0305M31-O3-029	03:05:19.481	−31:50:03.737	5.957	1.84 ± 0.42	373 ± 85
ASPIRE-J0305M31-O3-030	03:05:14.575	−31:51:46.999	5.815	4.20 ± 0.44	2316 ± 247
ASPIRE-J0305M31-O3-031	03:05:16.745	−31:51:10.141	5.662	1.92 ± 0.46	2758 ± 670
ASPIRE-J0305M31-O3-032	03:05:19.648	−31:50:31.465	5.448	3.06 ± 0.45	448 ± 66
ASPIRE-J0305M31-O3-033	03:05:19.666	−31:50:31.308	5.447	1.95 ± 0.52	253 ± 68
ASPIRE-J0305M31-O3-034	03:05:19.709	−31:50:30.986	5.442	10.43 ± 0.92	1922 ± 172
ASPIRE-J0305M31-O3-035	03:05:19.870	−31:51:19.826	5.432	4.14 ± 0.49	378 ± 44
ASPIRE-J0305M31-O3-036	03:05:19.122	−31:51:08.694	5.432	2.38 ± 0.32	203 ± 28
ASPIRE-J0305M31-O3-037	03:05:19.340	−31:51:13.606	5.432	4.32 ± 0.64	339 ± 51
ASPIRE-J0305M31-O3-038	03:05:16.856	−31:50:59.955	5.428	3.30 ± 0.51	491 ± 77
ASPIRE-J0305M31-O3-039	03:05:20.843	−31:50:50.277	5.399	2.74 ± 0.43	1228 ± 194
ASPIRE-J0305M31-O3-040	03:05:20.095	−31:51:05.726	5.395	3.09 ± 1.11	156 ± 56
ASPIRE-J0305M31-O3-041	03:05:20.113	−31:51:08.072	5.341	3.24 ± 1.34	4115 ± 1706

Notes.

[a] Galaxies spectroscopically confirmed from the ASPIRE program will be named as ASPIRE-JHHMMXDD-TT-NNN, where JHHMMXDD represents the quasar field name, TT denotes the galaxy type (i.e., O3 for [O III] emitters, HA for Hα emitters, and so on), and NNN represents the galaxy ID number.

[b] The redshift uncertainties of the galaxies are dominated by systematic wavelength zero-point offsets of the current spectral dispersion model, which would be improved with more JWST in-flight calibrations. To be conservative, we budget $\Delta z = 0.003$ for all galaxies identified in this work.

volume. The projected sky area is estimated to be 5.5 arcmin^2 (or 33.8 cMpc^2) at $z \sim 6.6$ in module A, and the length of the cylinder is estimated by assuming a line-of-sight range of ±1000 km s^{-1}, which delivers a cylinder volume of 637 cMpc^3. Such a cylinder is highlighted by the shaded region in the left panel of Figure 4. Using the 10 [O III] emitters, we measure the number density of the [O III] emitters in this structure to be $n_{\text{gal}} = 10^{-1.80^{+0.15}_{-0.16}}$ cMpc^{-3}. Since module A has better sensitivity than module B, and all [O III] emitters in the structure traced by the quasar are within module A (see Figure 1), we measure the average galaxy number density using the 24 field galaxies in module A (i.e., after excluding 10 [O III] emitters in the structure traced by the quasar). The effective survey area of the NIRCam/WFSS observations depends on

the wavelength of the line and thus the redshift of a given line emitter. We follow the method used by Sun et al. (2022b) to estimate the survey volume from $z = 5.2$ to 7.0 at a step of $\Delta z = 0.1$ and measure the effective survey volume of module A to be 20,813 cMpc^3 after excluding the volume of the cylinder described above. We then measure the volume density of the field galaxies to be $\bar{n}_{\text{gal}} = 10^{-2.94^{+0.10}_{-0.10}}$ Mpc^{-3}. These estimates indicate that the structure traced by the quasar has a galaxy overdensity of $\delta_{\text{gal}} = \frac{n_{\text{gal}}}{\bar{n}_{\text{gal}}} - 1 = 12.6^{+5.9}_{-5.0}$ within a cylinder volume of 637 cMpc^3. Note that we used a cylinder with a length of ±1000 km s^{-1} (or 18.8 cMpc) when estimating the galaxy overdensity. If we use the length (i.e., 8 cMpc) of the structure as determined by the 10 [O III] emitters, we would
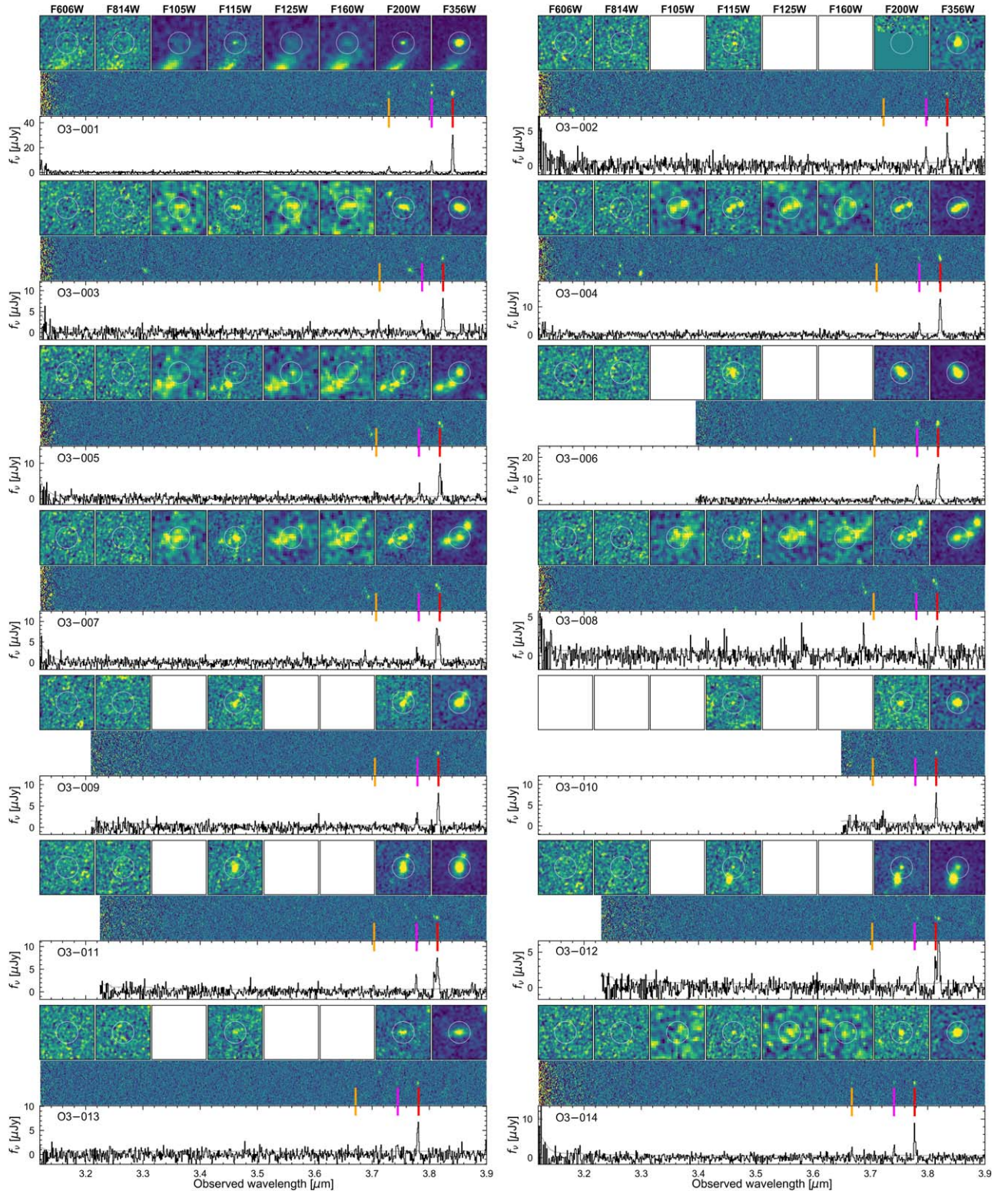
Figure 2. Image cutouts and spectra of the [O III] emitters. The cutouts from left to right show HST/F606W, HST/F814W, HST/F105W, JWST/F115W, HST/F125W, HST/F160W, JWST/F200W, and JWST/F356W. The size of the image cutouts is $2''0 \times 2''0$, and the radius of the white circles is $0''3$. All $z > 5.7$ [O III] emitters are undetected in the HST/F606W and HST/F814W images, as expected. The middle panels show the 2D coadded spectra, and the bottom panels show the optimally extracted spectrum for each galaxy. The Hβ, [O III] $\lambda4959$, and [O III] $\lambda5007$ are highlighted with orange, magenta, and red lines, respectively. The width of each 2D spectrum is 47 native pixels or $\sim3''0$. Note that we subtracted median-filtered continuum models for both 1D and 2D spectra here for visualization purposes. The spectra of the remaining [O III] emitters are shown at the end of the paper.

expect to have a galaxy overdensity close to 30 within a smaller volume. Additionally, the field galaxy density could be overestimated, given that this field contains two galaxy overdensities at $z = 5.4$ and 6.2. These estimates indicate that J0305−3150 traces one of the most overdense structures known in the early universe (e.g., Overzier 2022).
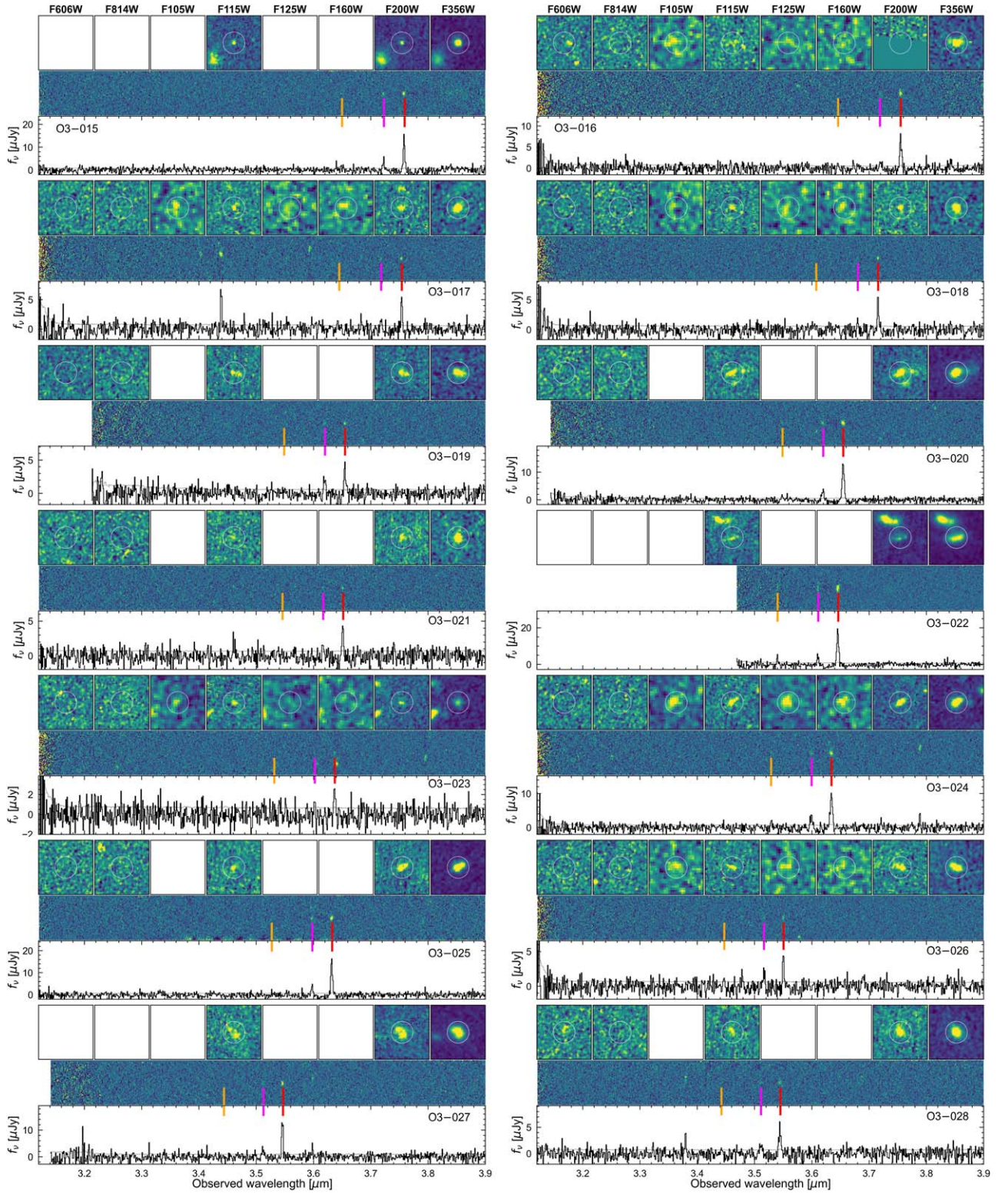
Figure 2. (Continued.)

To better understand this galaxy overdensity, we compare galaxy number counts with cosmological simulations. Using "zoom-in" cosmological simulations, Costa et al. (2014) and van der Vlugt & Costa (2019) showed that SMBHs with $M_{\rm BH} \sim 10^9 \, M_\odot$ form by $z = 6$ as long as they are hosted by massive halos with virial masses of $\approx (3\text{–}5) \times 10^{12} \, M_\odot$. We focus here on a suite of identical simulations targeting six such

halos, performed at eight times better mass resolution than Costa et al. (2014), such that the smallest resolved halos have a virial mass of $\approx 3 \times 10^7 \, M_\odot$. The masses of the black holes (BHs) hosted by the most massive galaxies in these halos range from 10^9 to $10^{10} \, M_\odot$ at $z = 6$. Following the empirical [O III]$-M_{\rm UV}$ relation presented in Matthee et al. (2022), we compute [O III] luminosities for all galaxies in the simulation at
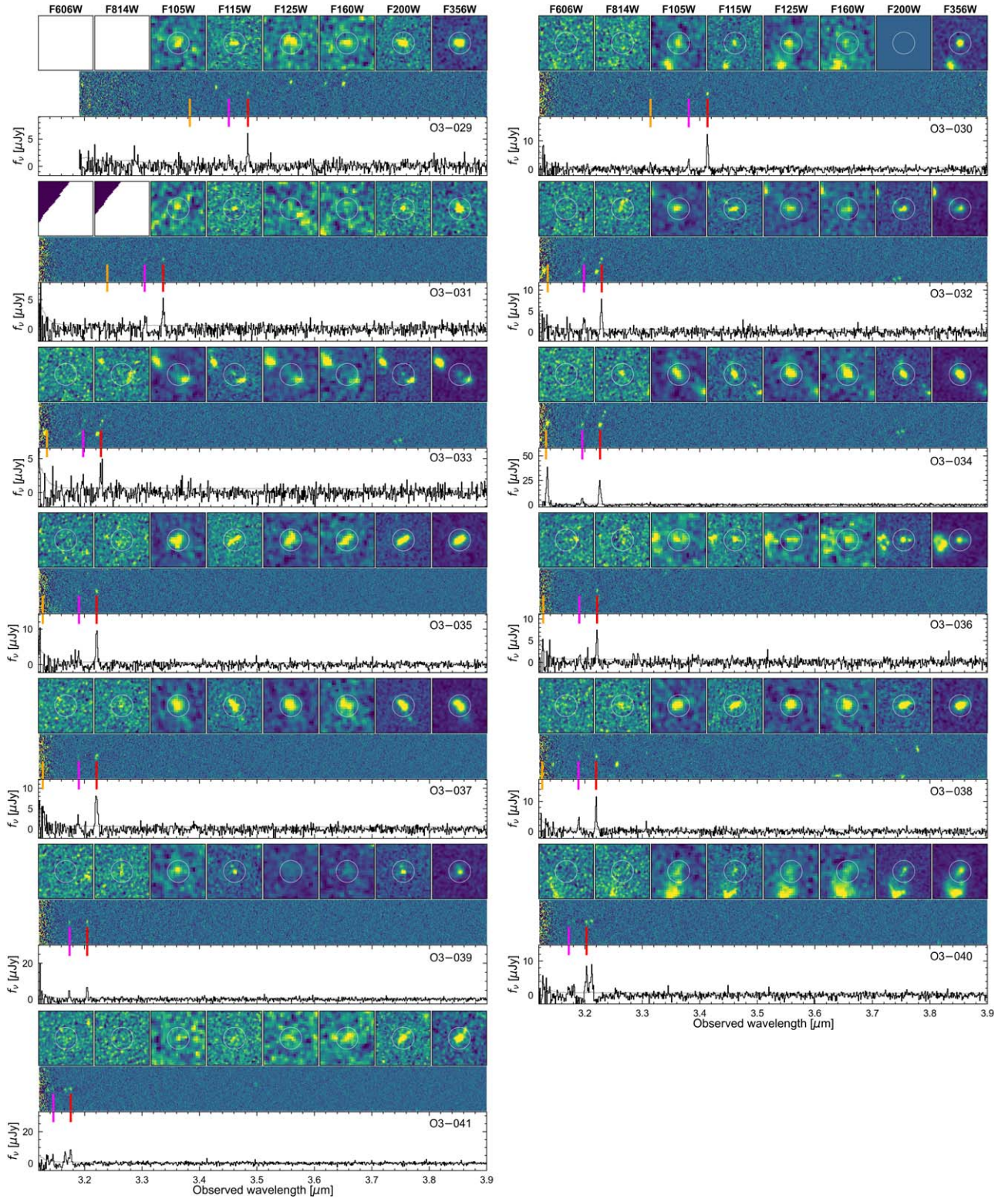
Figure 2. (Continued.)

$z = 6.6$ and then evaluate the total number of satellite galaxies with an unobscured [O III] luminosity $L_{[\text{O III}]\lambda5008\,\text{Å}} > 9.9 \times 10^{41}$ erg s^{-1} (5σ limit of our observation). Within a circular region of 33.8 cMpc^2, the satellite number count varies significantly, ranging from ≈ 10 to ≈ 36 with a mean of 21.5 across the halo sample. While our lower number count estimates are consistent with the number of satellites observed in this study, the simulations typically predict a factor of 2 higher number of satellites than found for J0305–3150. While this small discrepancy could indicate that the models overestimate the quasar halo mass, it could also be resolved if several of these satellites are significantly dust-obscured or the winds driven by stellar feedback are stronger than envisaged in the simulations (see Costa et al. 2014). Note that the virial
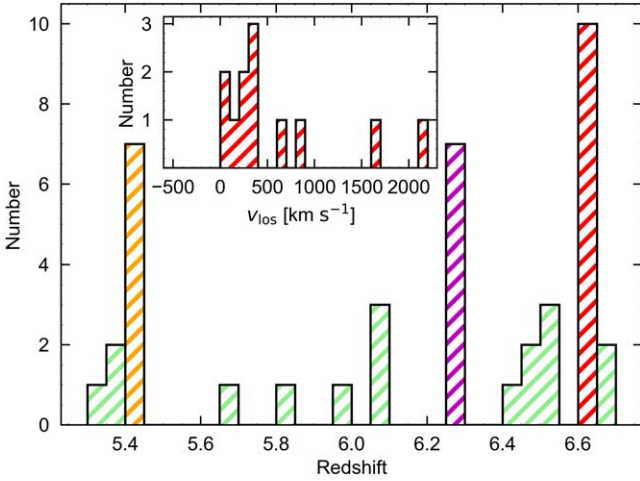
Figure 3. Redshift distribution of [O III] emitters. The [O III] emitters are strongly clustered in redshift space. There are obvious galaxy number excesses at $z \sim 5.4$, 6.2, and 6.6 in this field. The most significant excess in galaxy number appears at $z \sim 6.6$, the same redshift as the quasar. The inset shows the distribution of the line-of-sight velocities relative to the quasar of galaxies at $6.6 < z < 6.7$. Ten of the 12 galaxies at $z \sim 6.6$–6.7 have $v_{\rm los} < 1000$ km s^{-1} relative to the quasar. A positive velocity offset means that the galaxy has a higher redshift than the quasar. Limited by the precision of NIRCam/WFSS wavelength calibration, the redshifts of [O III] emitters could have a constant offset up to 0.003, as discussed in Section 2.3, which could explain the asymmetric distribution of $v_{\rm los}$.

masses of the six halos discussed here all lie in the range 10^{14}–$10^{15} M_\odot$ at $z = 0$, such that they all represent protocluster environments at $z = 6$. This suggests that the structure traced by J0305–3150 is consistent with a protocluster environment in the early universe and could eventually collapse into a massive galaxy cluster.

Furthermore, Habouzit et al. (2019) investigated the galaxy number counts around high-redshift quasars with Horizon-AGN. Limited by the volume, the biggest SMBH they could find in the simulation at $z \sim 6$ was a $10^{8.3} M_\odot$ SMBH that is hosted by a massive galaxy with a stellar mass of $M_\star = 10^{10.4} M_\odot$. In the field of this SMBH, they identified six (five) $M_\star \geqslant 10^8 M_\odot$ galaxies with a projected length of 50 (10) cMpc and within the survey area of our interest (5.5 arcmin^2 or 33.8 cMpc^2). Note that the 5σ limit of our [O III] line flux corresponds to $M_\star \simeq 10^8 M_\odot$ according to the [O III]$-M_{\rm UV}$ relation presented in Matthee et al. (2022) and the $M_{\rm UV}-M_\star$ relation at $z \sim 7$ from Stefanon et al. (2021), though both relations have large scatters. We confirmed these numbers by counting the galaxies ($M_\star \geqslant 10^8 M_\odot$) in a cylinder of length 18.8 cMpc and projected area of 33.8 cMpc^2 (see Figure 4) around the most massive SMBHs produced in the other cosmological simulations. At $z = 6$, the few SMBHs with $M_\star \geqslant 10^8 M_\odot$ are surrounded by a median of 3.5–4 galaxies (mean: 3.5–10.3) in SIMBA (Davé et al. 2019) and EAGLE (Schaye et al. 2015). These numbers are lower than the number of galaxies identified in the J0305–3150 field, but this is not surprising, as the quasar is powered by a more massive SMBH of $10^9 M_\odot$. BlueTides (Feng et al. 2016; Di Matteo et al. 2017) is the only current large-scale cosmological simulation with enough volume to produce several (seven) SMBHs with $\sim 10^9 M_\odot$. At $z = 7$ (the last output), these SMBHs are surrounded by a median of 15 galaxies with $M_\star \geqslant 10^8 M_\odot$ (from 11 to 66 galaxies). This is in good agreement with our present observation of J0305–3150's environment. We caution,

however, that all simulations of the field produce a variety of environments around SMBHs at high redshift. To increase statistics, we repeated the exercise with less massive SMBHs of $\sim 10^{7.5} M_\odot$ and found a large diversity in the number of surrounding galaxies with a median ranging from 2 to 21 (mean from 3.2 to 20.1) when considering Horizon-AGN (Dubois et al. 2014), Illustris (Vogelsberger et al. 2014), TNG100 (Pillepich et al. 2018), TNG300, EAGLE, SIMBA, Astrid (Bird et al. 2022; Ni et al. 2022), and BlueTides. These numbers significantly decrease when only galaxies with $M_\star \geqslant 10^{8.5}$ or $10^9 M_\odot$ are detectable in the SMBH field of view, making the detection of overdensities particularly challenging.

These comparisons indicate that the most massive BHs in cosmological simulations are usually traced by galaxy over-densities but with a broad range of galaxy numbers. In addition, shallow observations (i.e., only sensitive to galaxies with $M_\star \gtrsim 10^9 M_\odot$) could easily miss galaxy overdensities limited by the number of galaxies in the quasar fields. The completion of the ASPIRE program will enable a more systematic comparison between a large sample of quasar fields and the cosmological simulations by investigating galaxy numbers, galaxy velocity distribution, and quasar properties, which will deliver a more comprehensive understanding of the environment of the earliest SMBHs.

4.2. The Complex Vicinity of Quasar J0305–3150

Deep ALMA observations of J0305–3150 uncovered three [C II] 158 μm emitters in the quasar vicinity: galaxy C1 with a [C II] luminosity of $L_{\rm [C\,II]} = (4.7 \pm 0.5) \times 10^8 L_\odot$ at a projected distance of 2.0 pkpc, C2 with $L_{\rm [C\,II]} = (3.4 \pm 0.8) \times 10^8 L_\odot$ at a projected distance of 5.1 pkpc, and C3 with $L_{\rm [C\,II]} = (1.2 \pm 0.2) \times 10^9 L_\odot$ and a far-infrared luminosity of $L_{\rm FIR} = (1.3 \pm 0.3) \times 10^{12} L_\odot$ at a projected distance of 37.4 pkpc (Venemans et al. 2019). The positions of these galaxies are highlighted in the right panel of Figure 4, where we show the deep NIRCam imaging of the quasar vicinity (i.e., $\sim 60 \times 60$ pkpc^2 in the projected plane). Galaxy C1 is too close ($r < 0''.4$) to the quasar and cannot be detected by JWST without careful point-spread function (PSF) modeling, which will be discussed in a future work (J. Yang et al. 2023, in preparation). Galaxy C2 is detected by NIRCam in all three bands, though the flux is contaminated by the PSF spikes of the bright quasar. This galaxy is too faint to be detected in the WFSS observation. Galaxy C3 is remarkably bright in both [C II] and dust continuum ($f_{\rm 1mm} = 0.58 \pm 0.12$ mJy) but undetected in our deep NIRCam images with F115W ($f_{\rm 1.15\,\mu m, 3\sigma} < 8.9$ nJy), F200W ($f_{\rm 2.0\,\mu m, 3\sigma} < 4.1$ nJy), and F356W ($f_{\rm 3.56\,\mu m, 3\sigma} < 2.6$ nJy), which indicates that C3 is a dust-obscured galaxy similar to optically invisible dusty star-forming galaxies (DSFGs) found at lower redshifts (Wang et al. 2019b). We also note that the quasar's position measured from the NIRCam imaging is consistent with that measured from the ALMA observation with an offset of $0''.02$ (i.e., less than one-third of the resolution of both NIRCam and ALMA).

In addition to the three [C II] emitters, our JWST observations detected two $z \sim 6.6$ [O III] emitters in the quasar's immediate vicinity. Galaxy O3-003 has a projected distance of 18 pkpc and $v_{\rm los} = 870$ km s^{-1} relative to the quasar, and O3-004 has a projected distance of 11 pkpc and $v_{\rm los} = 670$ km s^{-1}. These two galaxies have [O III] $\lambda 5008$ luminosities of $L_{\rm [O\,III]} = (3.0 \pm 0.2) \times 10^{42}$ and $(6.2 \pm 0.2) \times 10^{42}$ erg s^{-1}, respectively. These two galaxies with bright [O III] emissions, however, are
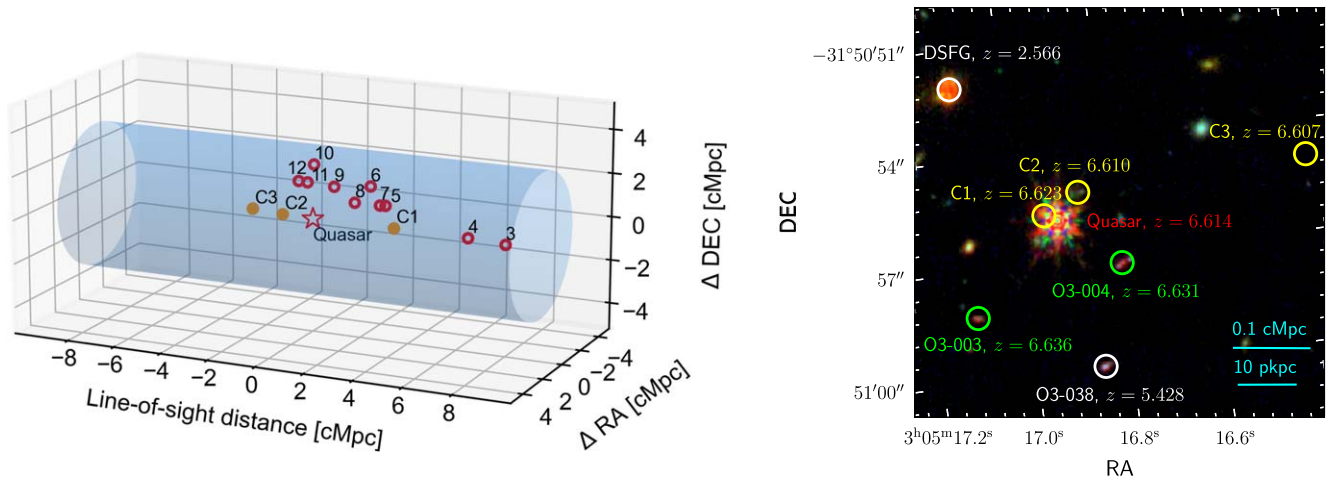
Figure 4. Left: 3D structure of the galaxy overdensity at $z = 6.6$. In this panel, we show both [O III] and [C II] emitters in the vicinity of the quasar. The blue shaded region highlights a cylinder volume with a line-of-sight length of 2000 km s^{-1} (or 18.8 cMpc) and a projected radius of 3.28 cMpc at $z = 6.6$ (corresponding to an effective area of 5.5 arcmin^2 in the projected plane). Right: immediate vicinity of quasar J0305–3150. The background is a RGB image made using NIRCam imaging in F115W (B), F200W (G), and F356W (R). Quasar J0305–3150 is surrounded by three [C II] emitters (C1, C2, and C3; Venemans et al. 2019) and two [O III] emitters (ASPIRE-J0305M31-O3-003 and ASPIRE-J0305M31-O3-004) with line-of-sight velocities relative to the quasar of $\Delta v_{los} < 1000$ km s^{-1}. Galaxy C3 is undetected in our deep JWST observations, which indicates that it is a DSFG. Galaxy [O III]-04 is also detected in Lyα (Farina et al. 2017). Two foreground galaxies are also shown with a DSFG at $z = 2.566$ and a [O III] emitter at $z = 5.428$.

undetected from the deep ALMA observations. We notice that galaxy O3-004 is also detected in both Hβ and Lyα ($z_{Ly\alpha} = 6.629$) from the NIRCam/WFSS and MUSE observations (Farina et al. 2017), respectively. The Hβ and Lyα line luminosities are measured to be $L_{H\beta} = (8.3 \pm 1.6) \times 10^{41}$ and $L_{Ly\alpha} = (2.1 \pm 0.2) \times 10^{42}$ erg s^{-1}, respectively. By assuming the standard Case B recombination with $T_e \sim 10^4$ K and $n_e = 10^2$ cm^{-3} and the absence of dust, we then estimate the Lyα escape fraction of this galaxy to be $f_{esc}^{Ly\alpha} = 10\%$, which is similar to other high-redshift galaxies found in a random field (i.e., a field without a luminous quasar; e.g., Hayes et al. 2011).

These observations show that the environment of the earliest SMBHs is very complex with diverse galaxy populations and indicates that the early evolution of galaxies around the quasar is not simultaneous. This could also partially explain why the existing observations solely based on rest-frame UV emissions or ALMA observations could not recover galaxy overdensities around a large number of quasars (see Overzier 2016, for a review).

4.3. Implications for the Formation and Environment of the Earliest SMBHs

One of the key open questions in cosmology is how the billion-solar-mass BHs formed within just several hundred million years after the Big Bang. Growing these SMBHs requires a very massive seed BH growing continuously at the Eddington limit and/or supercritical accretion on somewhat lighter seeds (e.g., Volonteri 2012; Yang et al. 2021). Theoretical models generally predict that the earliest billion-solar-mass BHs grew from remnants of quasi/supermassive stars (generically called direct-collapse BHs; e.g., Begelman et al. 2006; Inayoshi et al. 2020; Sassano et al. 2021) through cold flow accretion (e.g., Di Matteo et al. 2012) and were sometimes also aided by mergers (e.g., Li et al. 2007; Di Matteo et al. 2012; Dubois et al. 2012). This paradigm generally requires the seed to form in an overdense region, although not necessarily in the most massive halo of the region. This is because enhanced Lyman–Werner radiation from

nearby sources (e.g., Regan et al. 2017) or dynamical heating (e.g., Wise et al. 2019) is required to prevent gas fragmentation when it first collapses, and steady gas flows are needed to sustain a rapid accretion of gas to grow the seed BH during later stages (e.g., Latif et al. 2022).

However, previous observations only confirmed a few galaxy overdensities around the earliest SMBHs from extensive ground-based and HST observations (see Overzier 2016, for a review), which seems inconsistent with the theoretical expectations. In order to explain the lack of galaxy overdensity around quasars observed in these studies, several works proposed that strong radiation from quasars could heat the surrounding gas and suppress the formation of galaxies in the quasar vicinity (e.g., Utsumi et al. 2010) and/or the bulk of the galaxies in the quasar vicinity are dusty (e.g., Mazzucchelli et al. 2017). In this work, we found that J0305–3150, hosting an $\sim 10^9 M_\odot$ SMBH, accreting at the Eddington limit, and inhabiting a large-scale galaxy overdensity with both optical bright and dusty galaxies, is consistent with theoretical expectations. Earlier, shallower ground-based observations by Ota et al. (2018) did not find an LAE galaxy overdensity in the J0305–3150 field. These observations indicate that a lack of sensitivity, rather than radiation suppressing the formation of galaxies in the quasar vicinity, is responsible for missing galaxy overdensities in previous shallower observations (Habouzit et al. 2019; see also discussions in Section 4.1), at least for the case of J0305–3150. Therefore, we argue that it is still too early to judge whether the earliest SMBHs are generally good tracers of large-scale galaxy overdensities and whether quasar radiation could suppress galaxy formation in the quasar vicinity based on existing observations. The ASPIRE program, spectroscopically surveying 25 quasars in the EoR with excellent sensitivity and multiwavelength coverage, will enable us to eventually resolve these questions.

5. Summary

In this work, we provide a brief overview of the JWST ASPIRE program, which will perform a legacy galaxy redshift

survey in the fields of 25 reionization-era quasars using NIRCam/WFSS. From the early JWST observation of the field around the quasar J0305–3150, we discovered a filamentary structure traced by the quasar and 10 [O III] emitters at $z = 6.6$. This structure has a galaxy overdensity of $\delta_{\rm gal} = 12.6^{+5.9}_{-5.0}$ over a 637 cMpc^3 volume, making it one of the most overdense structures found in the early universe. By comparing with cosmological simulations, we argue that this filamentary structure traces an early overdensity, which could eventually evolve into a massive galaxy cluster. We also found that the most massive SMBHs in cosmological simulations generally trace galaxy overdensities but with a large variance on the galaxy numbers. This suggests that deep observations of a large sample of quasars (e.g., the ASPIRE program) would be essential for a comprehensive understanding of the cosmic environment of the earliest SMBHs. Together with archival multiwavelength observations, our JWST data indicate that the immediate vicinity of the quasar is very complex with a diverse galaxy population, including both UV-bright galaxies and DSFGs. These observations highlight the need for multi-wavelength characterizations of galaxies around the earliest SMBHs. In the field of J0305–3150, we also discovered 31 [O III] emitters at other redshifts, $5.3 < z < 6.7$, with half of them residing in two galaxy overdensities at $z = 5.4$ and 6.2. The serendipitous discovery of two galaxy overdensities in just one ASPIRE field indicates that high-redshift [O III] emitters are a strongly clustered population.

Facilities: ALMA, HST (ACS), HST (WFC3), JWST (NIRCam).

Software: astropy (Astropy Collaboration et al. 2018), Matplotlib (Hunter 2007), Numpy (Harris et al. 2020), Photutils (Bradley et al. 2022), Scipy (Virtanen et al. 2020), SExtractor (Bertin & Arnouts 1996).

ORCID iDs

Feige Wang ● https://orcid.org/0000-0002-7633-431X
Jinyi Yang ● https://orcid.org/0000-0001-5287-4242
Joseph F. Hennawi ● https://orcid.org/0000-0002-7054-4332
Xiaohui Fan ● https://orcid.org/0000-0003-3310-0131
Fengwu Sun ● https://orcid.org/0000-0002-4622-6617
Jaclyn B. Champagne ● https://orcid.org/0000-0002-6184-9097
Tiago Costa ● https://orcid.org/0000-0002-6748-2900
Melanie Habouzit ● https://orcid.org/0000-0003-4750-0187
Ryan Endsley ● https://orcid.org/0000-0003-4564-2771
Zihao Li ● https://orcid.org/0000-0001-5951-459X
Xiaojing Lin ● https://orcid.org/0000-0001-6052-4234
Romain A. Meyer ● https://orcid.org/0000-0001-5492-4522
Jan–Torge Schindler ● https://orcid.org/0000-0002-4544-8242
Yunjing Wu ● https://orcid.org/0000-0003-0111-8249
Eduardo Bañados ● https://orcid.org/0000-0002-2931-7824
Aaron J. Barth ● https://orcid.org/0000-0002-3026-0562
Aklant K. Bhowmick ● https://orcid.org/0000-0002-7080-2864
Laura Blecha ● https://orcid.org/0000-0002-2183-1087
Sarah Bosman ● https://orcid.org/0000-0001-8582-7012

Zheng Cai ⓘ https://orcid.org/0000-0001-8467-6478
Thomas Connor ⓘ https://orcid.org/0000-0002-7898-7664
Frederick B. Davies ⓘ https://orcid.org/0000-0003-0821-3644
Roberto Decarli ⓘ https://orcid.org/0000-0002-2662-8803
Gisella De Rosa ⓘ https://orcid.org/0000-0003-3242-7052
Alyssa B. Drake ⓘ https://orcid.org/0000-0002-0174-3362
Eiichi Egami ⓘ https://orcid.org/0000-0003-1344-9475
Anna-Christina Eilers ⓘ https://orcid.org/0000-0003-2895-6218
Analis E. Evans ⓘ https://orcid.org/0000-0003-0850-7749
Emanuele Paolo Farina ⓘ https://orcid.org/0000-0002-6822-2254
Zoltan Haiman ⓘ https://orcid.org/0000-0003-3633-5403
Linhua Jiang ⓘ https://orcid.org/0000-0003-4176-6486
Xiangyu Jin ⓘ https://orcid.org/0000-0002-5768-738X
Hyunsung D. Jun ⓘ https://orcid.org/0000-0003-1470-5901
Koki Kakiichi ⓘ https://orcid.org/0000-0001-6874-1321
Yana Khusanova ⓘ https://orcid.org/0000-0002-7220-397X
Girish Kulkarni ⓘ https://orcid.org/0000-0001-5829-4716
Mingyu Li ⓘ https://orcid.org/0000-0001-6251-649X
Weizhe Liu ⓘ https://orcid.org/0000-0003-3762-7344
Alessandro Lupi ⓘ https://orcid.org/0000-0001-6106-7821
Chiara Mazzucchelli ⓘ https://orcid.org/0000-0002-5941-5214
Masafusa Onoue ⓘ https://orcid.org/0000-0003-2984-6803
Maria A. Pudoka ⓘ https://orcid.org/0000-0003-4924-5941
Sofía Rojas-Ruiz ⓘ https://orcid.org/0000-0003-2349-9310
Yue Shen ⓘ https://orcid.org/0000-0003-1659-7035
Michael A. Strauss ⓘ https://orcid.org/0000-0002-0106-7755
Wei Leong Tee ⓘ https://orcid.org/0000-0003-0747-1780
Benny Trakhtenbrot ⓘ https://orcid.org/0000-0002-3683-7297
Maxime Trebitsch ⓘ https://orcid.org/0000-0002-6849-5375
Bram Venemans ⓘ https://orcid.org/0000-0001-9024-8322
Marta Volonteri ⓘ https://orcid.org/0000-0002-3216-1322
Fabian Walter ⓘ https://orcid.org/0000-0003-4793-7880
Zhang-Liang Xie ⓘ https://orcid.org/0000-0002-0125-6679
Minghao Yue ⓘ https://orcid.org/0000-0002-5367-8021
Haowen Zhang ⓘ https://orcid.org/0000-0002-4321-3538
Huanian Zhang ⓘ https://orcid.org/0000-0002-0123-9246
Siwei Zou ⓘ https://orcid.org/0000-0002-3983-6484

References

Astropy Collaboration, Price-Whelan, A. M., Sipőcz, B. M., et al. 2018, AJ, 156, 123
Bañados, E., Mazzucchelli, C., Momjian, E., et al. 2021, ApJ, 909, 80
Bañados, E., Venemans, B. P., Mazzucchelli, C., et al. 2018, Natur, 553, 473
Begelman, M. C., Volonteri, M., & Rees, M. J. 2006, MNRAS, 370, 289
Bertin, E., & Arnouts, S. 1996, A&AS, 117, 393
Bird, S., Ni, Y., Di Matteo, T., et al. 2022, MNRAS, 512, 3703
Bosman, S. E. I., Kakiichi, K., Meyer, R. A., et al. 2020, ApJ, 896, 49
Bradley, L., Sipocz, B., Robitaille, T., et al. 2022, astropy/photutils: v1.5.0, Zenodo, doi:10.5281/zenodo.6825092
Carnall, A. C., Begley, R., McLeod, D. J., et al. 2023, MNRAS, 518, L45
Champagne, J. B., Casey, C. M., & Finkelstein, S. L. 2023, arXiv:2304.10437
Costa, T., Sijacki, D., Trenti, M., & Haehnelt, M. G. 2014, MNRAS, 439, 2146

Curti, M., D'Eugenio, F., Carniani, S., et al. 2023, MNRAS, 518, 425
Davé, R., Anglés-Alcázar, D., Narayanan, D., et al. 2019, MNRAS, 486, 2827
Decarli, R., Walter, F., Venemans, B. P., et al. 2017, Natur, 545, 457
Dey, A., Schlegel, D. J., Lang, D., et al. 2019, AJ, 157, 168
Di Matteo, T., Croft, R. A. C., Feng, Y., Waters, D., & Wilkins, S. 2017, MNRAS, 467, 4243
Di Matteo, T., Khandai, N., DeGraf, C., et al. 2012, ApJL, 745, L29
Di Matteo, T., Springel, V., & Hernquist, L. 2005, Natur, 433, 604
Dubois, Y., Pichon, C., Haehnelt, M., et al. 2012, MNRAS, 423, 3616
Dubois, Y., Pichon, C., Welker, C., et al. 2014, MNRAS, 444, 1453
Farina, E. P., Venemans, B. P., Decarli, R., et al. 2017, ApJ, 848, 78
Feng, Y., Di-Matteo, T., Croft, R. A., et al. 2016, MNRAS, 455, 2778
Greene, T. P., Kelly, D. M., Stansberry, J., et al. 2017, JATIS, 3, 035001
Habouzit, M., Volonteri, M., Somerville, R. S., et al. 2019, MNRAS, 489, 1206
Harris, C. R., Millman, K. J., van der Walt, S. J., et al. 2020, Natur, 585, 357
Hayes, M., Schaerer, D., Östlin, G., et al. 2011, ApJ, 730, 8
Horne, K. 1986, PASP, 98, 609
Hunter, J. D. 2007, CSE, 9, 90
Inayoshi, K., Visbal, E., & Haiman, Z. 2020, ARA&A, 58, 27
Kashino, D., Lilly, S. J., Matthee, J., et al. 2022, arXiv:2211.08254
Kim, S., Stiavelli, M., Trenti, M., et al. 2009, ApJ, 695, 809
Latif, M. A., Whalen, D. J., Khochfar, S., Herrington, N. P., & Woods, T. E. 2022, Natur, 607, 48
Li, Y., Hernquist, L., Robertson, B., et al. 2007, ApJ, 665, 187
Matthee, J., Mackenzie, R., Simcoe, R. A., et al. 2022, arXiv:2211.08255
Mazzucchelli, C., Bañados, E., Decarli, R., et al. 2017, ApJ, 834, 83
Meyer, R. A., Decarli, R., Walter, F., et al. 2022, ApJ, 927, 141
Mignoli, M., Gilli, R., Decarli, R., et al. 2020, A&A, 642, L1
Morselli, L., Mignoli, M., Gilli, R., et al. 2014, A&A, 568, A1
Ni, Y., Di Matteo, T., Bird, S., et al. 2022, MNRAS, 513, 670
Ota, K., Venemans, B. P., Taniguchi, Y., et al. 2018, ApJ, 856, 109
Overzier, R. A. 2016, A&ARv, 24, 14
Overzier, R. A. 2022, ApJ, 926, 114
Overzier, R. A., Guo, Q., Kauffmann, G., et al. 2009, MNRAS, 394, 577
Pillepich, A., Nelson, D., Hernquist, L., et al. 2018, MNRAS, 475, 648
Prochaska, J., Hennawi, J., Westfall, K., et al. 2020, JOSS, 5, 2308
Regan, J. A., Visbal, E., Wise, J. H., et al. 2017, NatAs, 1, 0075
Rieke, M. J., Kelly, D., & Horner, S. 2005, Proc. SPIE, 5904, 1
Sassano, F., Schneider, R., Valiante, R., et al. 2021, MNRAS, 506, 613
Schaye, J., Crain, R. A., Bower, R. G., et al. 2015, MNRAS, 446, 521
Schlawin, E., Leisenring, J., Misselt, K., et al. 2020, AJ, 160, 231
Simpson, C., Mortlock, D., Warren, S., et al. 2014, MNRAS, 442, 3454
Springel, V., White, S. D. M., Jenkins, A., et al. 2005, Natur, 435, 629
Stefanon, M., Bouwens, R. J., Labbé, I., et al. 2021, ApJ, 922, 29
Sun, F., Egami, E., Pirzkal, N., et al. 2022a, arXiv:2209.03374
Sun, F., Egami, E., Pirzkal, N., et al. 2022b, ApJL, 936, L8
Utsumi, Y., Goto, T., Kashikawa, N., et al. 2010, ApJ, 721, 1680
van der Vlugt, D., & Costa, T. 2019, MNRAS, 490, 4918
Venemans, B. P., Findlay, J. R., Sutherland, W. J., et al. 2013, ApJ, 779, 24
Venemans, B. P., Neeleman, M., Walter, F., et al. 2019, ApJL, 874, L30
Virtanen, P., Gommers, R., Oliphant, T. E., et al. 2020, NatMe, 17, 261
Vogelsberger, M., Genel, S., Springel, V., et al. 2014, MNRAS, 444, 1518
Volonteri, M. 2012, Sci, 337, 544
Wang, F., Yang, J., Fan, X., et al. 2019a, ApJ, 884, 30
Wang, F., Yang, J., Fan, X., et al. 2021, ApJL, 907, L1
Wang, T., Schreiber, C., Elbaz, D., et al. 2019b, Natur, 572, 211
Willott, C. J., Percival, W. J., McLure, R. J., et al. 2005, ApJ, 626, 657
Wise, J. H., Regan, J. A., O'Shea, B. W., et al. 2019, Natur, 566, 85
Wu, X.-B., Wang, F., Fan, X., et al. 2015, Natur, 518, 512
Yang, J., Wang, F., Fan, X., et al. 2019, AJ, 157, 236
Yang, J., Wang, F., Fan, X., et al. 2020a, ApJL, 897, L14
Yang, J., Wang, F., Fan, X., et al. 2020b, ApJ, 904, 26
Yang, J., Wang, F., Fan, X., et al. 2021, ApJ, 923, 262
Yang, J., Wang, F., Fan, X., et al. 2023, arXiv:2304.09888
Zheng, W., Overzier, R. A., Bouwens, R. J., et al. 2006, ApJ, 640, 574